PCCP

PAPER

View Article Online
View Journal

Cite this: DOI: 10.1039/d6cp00607h

Deep eutectic solvent-assisted hydrothermal synthesis of chitosan-based nanohybrid films functionalized with silver-decorated tungsten oxide

Shephrah Olubusola Ogungbesan,*[a] Oluwaseun Hanah Anselm,[b] Eduardo Buxaderas,[c] Yanina Moglie,[c] César Saldías,[d] Mulenga Kalulu,[a] Rosemary Anwuli Adedokun,[e] Enock Olugbenga Dare,[f] Michael Olawale Daramola,[g] David Díaz Díaz*[hi] and Guodong Fu*[a]

This study presents the fabrication and characterization of chitosan-based nanohybrid films incorporating silver-decorated tungsten oxide (Ct–AgWO$_3$). In this work, the deep eutectic solvent-assisted hydrothermal synthesis of WO$_3$ nanoparticles was combined with *in situ* silver decoration and chitosan reduction to synthesize a nanohybrid film. The effects of reaction time on the structural, morphological, and functional properties of the nanohybrid films were investigated over time. The resulting nanohybrid film was characterized using UV-vis spectroscopy, FESEM, EDX, FTIR, XPS, Raman spectroscopy, TGA, and photoluminescence. Morphological analysis revealed an evolution from clustered particulates at 30 min to better-dispersed nanoparticles after 6 h, with particle sizes between *ca.* 21 and 48 nm. XPS analysis of the nanofilm confirmed the presence of the W^{6+} oxidation state and the successful silver decoration. Moreover, the Raman spectra revealed a monoclinic WO$_3$ crystal structure and enhanced electronic properties due to the oxygen vacancies created by Ag decoration. The degree of degradation resistance was greater than that of the chitosan–WO$_3$ films without silver decoration, as revealed by the thermal analysis data.

Received 19th February 2026,
Accepted 26th May 2026

DOI: 10.1039/d6cp00607h

rsc.li/pccp

Introduction

There has recently been an increase in the use of n-type semiconductors in gas sensing, pollution control, drug delivery, biosensors, and anticancer and antimicrobial activities, among other applications.[1–3] Tungsten trioxide (WO$_3$) is one of the most frequently used n-type semiconductors and is widely applied in the biomedical field because of its tunable energy band gap of less than 3.0 eV, which makes it suitable for visible light absorption, and it has several notable physicochemical properties, such as optochromism, electrochromism, gasochromism, near-infrared (NIR) light absorption, and conversion into thermal energy.[4–6] Its high resistance to corrosion is attributed to tungsten having a highly oxidative state (+6), which prevents further electron loss.[7] The crystal structure of WO$_3$ varies with preparation method and temperature, exhibiting phases such as orthorhombic, monoclinic, triclinic, and tetragonal.[8] At room temperature, WO$_3$ is most stable in the monoclinic phase, which is crucial for maintaining its optical and electronic properties in biomedical applications.[9] Additionally, nonstoichiometric tungsten oxides are of significant interest because of their enhanced electrical conductivity,

[a] School of Chemistry and Chemical Engineering, Southeast University, 2 Southeast University Road, 211189 Nanjing, P. R. China. E-mail: 233189910@seu.edu.cn, fu7352@seu.edu.cn
[b] College of Science and Information Technology, Tai Solarin University of Education, PMB 2118, Ijebu-Ode, Ogun State, Nigeria
[c] Instituto de Química del Sur, INQUISUR (CONICET-UNS), Departamento de Química, Universidad Nacional del Sur, Avda. Alem 1253, 8000 Bahía Blanca, Argentina
[d] Departamento de Química Física, Facultad de Química y de Farmacia, Pontifica Universidad Católica de Chile, Chile
[e] Department of Chemistry, Chrisland University Abeokuta, KM 3, Ajebo Road after FMC, 23409 Abeokuta, Nigeria
[f] College of Physical Sciences, Federal University of Agriculture Abeokuta, PMB 2240, Alabata Road, Abeokuta, Ogun State, Nigeria
[g] Sustainable Energy and Environment Research Group (SEERG), Department of Chemical Engineering, University of Pretoria, Hatfield 0028, Pretoria, South Africa
[h] AFM-NANO, Instituto Universitario de Bio-Orgánica Antonio González (IUBO-AG), Universidad de La Laguna, Avda. Astrofísico Francisco Sánchez 2, La Laguna 38206, Spain. E-mail: dddiazdiaz@ull.edu.es
[i] Departamento de Química Orgánica, Universidad de La Laguna, Avda. Astrofísico Francisco Sánchez 3, La Laguna 38206, Spain

superior NIR photothermal conversion ability, and narrower band gap caused by oxygen vacancies.[10] Both stoichiometric and nonstoichiometric tungsten oxides are small, environmentally friendly, and cost-effective, making them suitable for various electrochemical and biomedical applications, including temperature sensors, photoelectrodes, visible light photocatalysts, biosensors, and agents for photothermal and photodynamic therapy.[11]

The physicochemical properties of WO_3 nanomaterials can be fine-tuned by adjusting their dimensions, crystal structure, and morphology, which is crucial for enhancing their biomedical and chemical applications.[12] There are various techniques to alter their nanoscale geometry. However, introducing dopants (such as Pt, Au, Ag, Zn, Fe, Cr, Sn, or Bi) into the WO_3 lattice is the simplest method to achieve the desired properties.[13] For example, treatment with Cs, Bi, or Rb increases the absorption of NIR light by WO_3 nanoparticles and their efficient heat transfer.[14] Decoration with magnetically active metal ions such as Mn^{2+} or Gd^{3+} is useful for designing MRI-guided photothermal and photodynamic therapies.[15–17] Moreover, the formation of conjugates or hybrids with other semiconductor compounds (such as the metal oxides SnO_2, Co_3O_4, Fe_2O_3, ZnO, TiO_2, and Cu_2O, CdS, graphene oxide, and carbon dots) enhances the production of free radicals under exposure to visible light. Additionally, strong absorbance and good photoconversion effectiveness are made possible by the conjugation of WO_3 with TeO_2 in the first near-infrared region between 650 and 950 nm and in the second between 1000 and 1350 nm.[1]

Given the growing use of metal-decorated and hybrid WO_3 nanoparticles in biomedicine, developing new synthetic strategies to increase their production and efficiency is crucial. The known efficiency of silver nanoparticles in biomedical applications, such as cancer theragnostics, anti-inflammatory, antibacterial, antiplatelet, antiangiogenic, antiviral, and antifungal activities, tissue engineering, wound healing, dental care, and drug delivery, among others, is considered.[18] Silver nanoparticles are postulated to exert microbial effects through damage to the membranes of microbes and damage to the subcellular structure. Despite their known antimicrobial efficacy, silver nanoparticles face challenges such as instability, cytotoxicity to healthy cells, and microbial resistance at high concentrations, necessitating their optimization. Additionally, the instability of silver nanoparticles, which is linked to agglomeration, can be prevented by decorating them with metal oxides or incorporating them into polymeric materials.[19,20] The decoration of WO_3 can increasingly generate valence electrons, which in turn modulate the efficiency and reactivity of the nanocomposite.

While numerous studies have focused on the synthesis, properties, and various applications of tungsten oxide nanoparticles, to the best of our knowledge, there have been no reports on silver-decorated tungsten oxide chitosan nanohybrid films. Silver nanoparticles (AgNPs) are unique among metallic nanomaterials and have a wide range of applications because of their distinct physicochemical characteristics (such as optical, thermal, and electrical conductivity), and the introduction of a small amount of silver nanoparticles into the semiconductor crystal of WO_3 nanoparticles, *via* nontoxic, biodegradable, biocompatible and bioavailable chitosan as a reducing agent, will greatly increase their optical, conductivity and photocatalytic properties, among other properties. Research conducted in the past has shown that silver nanoparticles are effective for antimicrobial activity,[21] and that WO_3 is effective for photocatalytic activity,[22] but the combination of silver nanoparticles in a chitosan biopolymer matrix has not been studied. This novel combination may indeed improve the stability of silver nanoparticles through metal oxide decoration, increase the photocatalytic efficiency of WO_3 *via* the plasmonic effect of silver, and provide a biocompatible carrier system through the chitosan matrix. To this end, this study presents the fabrication of WO_3 NPs *via* deep eutectic solvent DES-assisted hydrothermal synthesis, *in situ* decoration and chitosan reduction of silver ions. The resulting slurry was subsequently cast to form a silver-decorated tungsten nanoparticle film *via* the solvent casting method. A green method was employed in this fabrication process; hence, the study was carried out without the use of harmful chemicals. The working principle of this nanohybrid system is based on cooperation among its three main constituents. The amino and hydroxyl groups of chitosan act as reducing and stabilizing agents, which coordinate with WO_3 and reduce the Ag ions into nanoparticles. The inclusion of silver in the WO_3 system is expected to influence the electronic structure, potentially introducing oxygen vacancies and modifying the band gap, which may affect the absorption of visible light. Therefore, this electronic modification, together with the possible formation of Ag–WO_3 interfaces, may influence charge transfer processes and consequently affect the photocatalytic behavior and consequent antibacterial efficacy through the increased generation of reactive oxygen species. The creation of this nanohybrid system not only adds to the list of antibacterial materials but also provides a basis for tunable antimicrobial functionality without excessive amounts of silver, which can hamper bacterial resistance and cause cytotoxic effects in existing silver systems.

Materials and methods

Materials

All the materials used in this study were of analytical grade, were supplied by Aladdin Inc. (Shanghai, China) and were used as purchased without further purification. The materials used included sodium tungstate dihydrate ($Na_2WO_4{\cdot}2H_2O$ $\geq$99.95%), sodium chloride (NaCl $\geq$99.5%), glacial acetic acid 100%, ethylene glycol (EG $\geq$99.8%), choline chloride (ChCl $>$98%), and silver nitrate ($AgNO_3$). Chitosan with a degree of deacetylation $\geq$95%, was acquired from BeyoClick, China. Double-distilled water was used in the preparation of all aqueous solutions.

Synthesis of WO_3 NPs and the Ag-decorated WO_3-NP film

Tungsten oxide nanoparticles were prepared as described in our previous work, with slight modifications.[23] Briefly, prior to

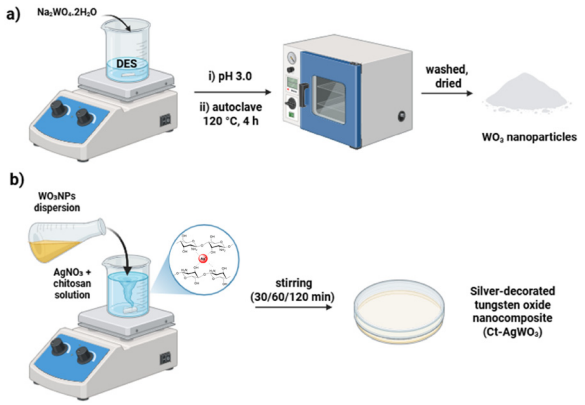

Scheme 1 . Schematic illustration of the fabrication of the Ct–$AgWO_3$ nanohybrid film: (a) synthesis of WO_3 nanoparticles. (b) Synthesis of silver-decorated tungsten oxide nanocomposite (Ct–$AgWO_3$). Film thickness = 0.011 ± 0.001 mm.

the preparation of WO_3, DES was prepared by dissolving 0.811 g of ChCl in 50 mL of 0.130 M NaCl and 2.701 mL of ethylene glycol (EG) and vigorously stirred for 5 min at 80 °C until all the particles were completely dissolved. After the formation of the clear DES, 0.851 g of $Na_2WO_4{\cdot}2H_2O$ was added under continuous stirring. The solution was maintained at pH 3.0 by the gradual addition of acetic acid to optimize nanoparticle formation, and the reaction flask was covered with foil to prevent light-induced reactions. The solution was then placed in an autoclave oven at 120 °C for 4 h for the hydrothermal reaction (Scheme 1). The resulting whitish particles in the reaction flask were collected and washed with ethanol and water. The resulting tungsten oxide nanoparticles were dried and stored for subsequent use.[24] A total of 0.356 g of the synthesized WO_3 nanoparticles was dispersed in 1 mL of H_2O. A mixture of 20 mL of 0.1% $AgNO_3$ and 100 mL of 1% chitosan slurry was added subsequently, and the mixture was stirred. After 30 min, 120 min and 360 min, the slurry samples were collected and cast in Petri dishes. Film thickness was determined using a micrometer thickness gauge. Measurements were performed at least three times, and the mean values were reported along with the corresponding error.

Characterization

The optical properties of the chitosan-based nanocomposite films containing tungsten oxide nanoparticles were evaluated using a molecular fluorescence spectrometer (FluoroMax-Plus) and a UV–vis spectrophotometer (UV-2600) in the 200–900 nm range. Thermogravimetric analysis (TG209 F3) was carried out to investigate the thermal stability of the films. The morphology and elemental composition of the nanocomposites were examined by field emission scanning electron microscopy coupled with energy-dispersive X-ray spectroscopy (FESEM/EDX, Nova NanoSEM450). Functional groups, chemical interactions, and structural features were analyzed using Fourier transform infrared spectroscopy (FTIR, Nicolet iS50) and micro-Raman spectroscopy (XploRA PLUS).

Results and discussion

Scheme 1 illustrates the synthesis processes of the chitosan silver-decorated tungsten oxide nanohybrid film (Ct–$AgWO_3$). Initially, WO_3 nanoparticles were synthesized using a deep eutectic solvent under acidic conditions, followed by hydrothermal treatment, where the pH of the Na_2WO_4 precursor solution was adjusted to 3.0. The details of the mechanism of the synthesis of WO_3-NPs has been reported previously.[15] Chitosan was dissolved in diluted glacial acetic acid to form a transparent slurry, which acts as both a stabilizing matrix and a reducing agent for the conversion of Ag^+ ions into silver nanoparticles. Under acidic conditions, the amine groups of chitosan become protonated, facilitating the coordination of WO_3 nanoparticles through $-NH_2$ and hydroxyl functional groups. Simultaneously, Ag^+ ions were reduced by the amino groups of chitosan and stabilized within the chitosan matrix.[25]

The resulting slurry was cast and dried at room temperature after reaction times of 30 min, 2 h, and 6 h. These reaction times were selected to investigate the time-dependent evolution of the Ag/WO_3–chitosan nanocomposites. At 30 min, the presence of relatively small particles with limited crystallinity suggests an initial nucleation stage of Ag and WO_3 nanoparticles and their early interaction with the chitosan matrix. At an intermediate reaction time of 2 h, enhanced nanoparticle growth and improved dispersion are observed, while the data suggests the presence of stronger interfacial interactions, as supported by morphological and spectroscopic analyses, which may be associated with the improved mechanical and optical behavior of the films. Extending the reaction time to 6 h is associated with further particle growth and increased crystallinity, leading to larger nanoparticles and suggesting more robust interfacial interactions, which may contribute to enhanced thermal stability and improved overall functional performance for the nanocomposites.

UV-vis analysis

The optical characteristics of the synthesized nanohybrid films formed after 30 min, 2 h and 6 h of reaction, as determined *via* diffuse reflectance spectrophotometry, are illustrated in Fig. 1a–c. The spectra of the nanohybrid films show absorption peaks between 400 and 500 nm. This indicates that induced charge transfer occurred between the O 2p and W 5d orbitals.[26] The reduction in reflectance with time from 30 min to 6 h denotes the time-dependent nature of silver ion reduction by the chitosan slurry, which directly influences nanoparticle formation and optical properties (Fig. 1a and b).

This demonstrates the progressive evolution of silver nanoparticle formation through chitosan-mediated reduction. This finding aligns with those of Din and co-workers[27] on silver-decorated semiconductor systems, although the present system shows enhanced absorption characteristics, possibly due to the presence of chitosan. As the particle size increases, the absorption edge migrates towards longer wavelengths. Particle size and energy gap are two major parameters that affect light absorption.[28]

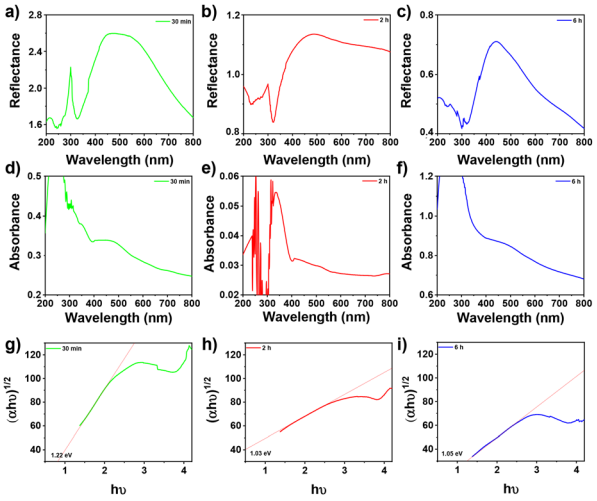

Fig. 1 (a)–(c) Diffuse reflectance spectra, (d)–(f) UV-vis absorption spectra (200–900 nm), and (g)–(i) Tauc band gap plots of the prepared Ct–AgWO_3 nanohybrid films at reaction times of 30 min (green line), 2 h (red line), and 6 h (blue line).

Fig. 1d–f show the absorption spectra of the three film samples. As the degree of decoration (Ag) and nanoparticle formation increased, the absorption edge migrated towards longer wavelengths. UV-vis absorption spectra provide insights into the development of electronic transitions and the formation of nanoparticles within the nanohybrid films. Initially, after 30 min (green line), the absorption peak is relatively weak, indicating the early stages of silver ion reduction and its interaction with the chitosan matrix. At 2 h (red line), the absorption intensity increases, with a more pronounced peak at approximately 400 nm, suggesting the occurrence of WO_3-related electronic transitions and the formation of Ag nanoparticles *via* localized surface plasmon resonance (LSPR). As the reaction progresses to 6 h (blue line), the absorption band broadens and undergoes a redshift, indicative of enhanced silver incorporation and possible nanoparticle aggregation. The gradual integration of silver into the WO_3 matrix modifies the electronic structure and optical properties of the nanohybrid film, as evidenced by the increasing absorption intensity and peak shift over time. These observations suggest that an extended reaction time improves the efficiency of silver incorporation and significantly influences the optoelectronic behavior of the material.

It should be noted that the distinct shape observed for the 2 h sample may be associated with differences in nanoparticle distribution and surface morphology, as suggested by SEM analysis. This intermediate stage of growth may lead to variations in light scattering and optical response compared to the 30 min and 6 h samples. Moreover, the spectral region below 300 nm exhibits strong and irregular features, which can be attributed to instrumental limitations and enhanced light scattering effects at high absorption energies. Such effects are commonly observed in nanostructured films and may lead to signal distortion in this spectral range. It is also important to consider that absorbance measurements in nanostructured films are highly sensitive to film thickness, surface roughness, and light scattering effects, which can influence the spectral shape. This may explain the apparent differences between the absorbance and reflectance data of these materials.

The optical band gap (E_g) was estimated using Tauc plots based on the Kubelka–Munk function derived from diffuse reflectance data, assuming an indirect allowed transition for WO_3. The band gap values were obtained by extrapolating the linear region of the $(F(R)\cdot h\nu)^{1/2}$ *vs.* $h\nu$ plots to the energy axis. It should be noted that the determination of E_g is subject to uncertainty due to the selection of the linear fitting region and baseline variations, with an estimated uncertainty of approximately $\pm$0.05–0.10 eV. The decrease in the energy band gap (Fig. 1g–i) observed in the films synthesized at 30 min, 2 h, and 6 h suggests the formation of localized states within the band gap, induced by the incorporation of Ag into the WO_3–chitosan matrix. These localized states facilitate electronic transitions at lower energy levels, contributing to the observed narrowing of the band gap. As the reaction time increases, the enhanced incorporation of silver and interaction with WO_3 are likely to lead to improved charge carrier mobility, which in turn can enhance the photocatalytic efficiency and optoelectronic performance of the material. These results suggest that incorporation of Ag and structural evolution may influence the optical properties of the system. Additionally, this decrease in the energy band gap over time suggests successful silver decoration, potentially enhancing the photocatalytic activity of the material in biological systems.[29] For comparison, the optical band gap of WO_3 was independently estimated from UV-vis absorption data to be approximately 2.66 eV, which is consistent with reported values for WO_3 in the range of 2.5–3.0 eV.[4]

The reduced band gap can be attributed to multiple factors. Chitosan, acting as both stabilizing and reducing agent, introduces additional electronic interactions within the nanohybrid system, potentially modifying its electronic structure and contributing to narrowing of the band gap[30] The hydroxyl (–OH) and amino ($-NH_2$) functional groups in chitosan can coordinate with WO_3 and Ag, modifying the electronic structure and potentially generating mid-gap states that contribute to reduction of the band gap. Additionally, the extent of Ag incorporation plays a crucial role, as higher silver concentrations can enhance localized surface plasmon resonance (LSPR) effects. The interaction between Ag nanoparticles and WO_3 can introduce impurity states within the band structure, further lowering the optical band gap and influencing the optoelectronic properties of the material.[31]

Another critical factor to consider is the formation of oxygen vacancies, induced by the incorporation of Ag into the WO_3 structure.[32] These vacancies act as donor states within the band gap, introducing additional energy levels that contribute to narrowing of the band gap. Moreover, the extended reaction time during synthesis influences crystallinity, particle size, and the extent of Ag incorporation. A longer reaction time enhances decoration efficiency and strengthens electronic interactions, further promoting reduction of the band gap.[33]

Additionally, the hybridization of electronic states, arising from the interaction of WO_3 with the functional groups of chitosan, along with Ag reduction and capping, can modify both the conduction and valence bands, thereby altering the overall electronic structure of the nanocomposite.

The observed band gap reduction can also be attributed to the structural and morphological characteristics of the material, including its crystallinity, nanostructure size, and interfacial interactions among Ag, WO_3, and chitosan. A less ordered structure, increased surface states, or modifications in electronic transitions can shift the absorption edge, leading to further narrowing of the band gap. Nevertheless, a direct comparison with WO_3 or Ct–WO_3 reference samples would be required to isolate the specific effect of Ag incorporation, which is beyond the scope of the present study.

Morphological analysis

Field emission scanning electron microscopy (FESEM) was employed to examine the morphology of the nanohybrid film samples. Fig. 2 shows the corresponding micrographs and particle size distributions. All three film samples exhibited the formation of nanoscale structures attributed to WO_3 nanoparticles decorated with Ag and embedded within the chitosan matrix, as supported by SEM observations in conjunction with EDX mapping, XPS, and Raman analyses. In t context, the term ''nanoparticles'' refers to WO_3-based nanoscale domains with Ag decoration distributed within the chitosan matrix.

The nanohybrid film obtained after 30 min of reaction (Fig. 2a) showed noticeable particle aggregation and irregular shapes. In contrast, the Ct–$AgWO_3$ nanohybrid film formed after 2 h of reaction displayed smaller and more dispersed nanoparticles (Fig. 2b). However, the particle density at this stage was lower than that observed in the nanohybrid film synthesized after 6 h, which exhibited well-dispersed, densely populated nanoparticles with a more defined spherical morphology (Fig. 2c). This morphology suggests uniform particle growth and reduction in surface energy, which are essential for enhanced dispersion within the chitosan matrix.

The average particle size of the film synthesized after 30 min was 48.03 nm, whereas that of the film obtained after 2 h of reaction was 29.29 nm. This difference in particle size may be attributed to incomplete dispersion of the nanoparticles within the chitosan matrix at shorter reaction times, resulting in particle aggregation in the 30 min sample. The particle size distribution of the 30 min film revealed a broad range of sizes, indicating a high degree of polydispersity. After 2 h of reaction, the total number of nanoparticles increased and the average particle size decreased to 21.29 nm (Fig. 2b), which may be attributed to the increased reduction of silver ions by chitosan. The higher nanoparticle density in the 6 h film sample indicates enhanced nanoparticle formation, while the increase in the average particle size at this stage can be attributed to the successful decoration of a larger number of WO_3 nanoparticles by silver atoms. This significant increase in particle density suggests that the reduction of silver ions to silver-decorated tungsten oxide nanocomposite are time-dependent processes.

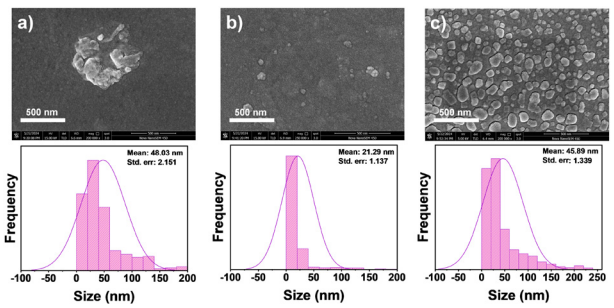

Fig. 2 SEM micrographs and corresponding particle size distribution curves of the Ct–$AgWO_3$ films prepared after (a) 30 min, (b) 2 h, and (c) 6 h of reaction.

The formation of Ct–$AgWO_3$ nanohybrid films likely follows a nucleation and growth mechanism driven by specific chemical interactions among the components. The aggregation observed at the initial reaction stage (30 min) can be ascribed to the rapid reduction of silver ions by the amino group of chitosan, consistent with the mechanism proposed by Zaheer,[17,34] in which $-NH_2$ groups act as both reducing and stabilizing agents.

The subsequent evolution toward well-dispersed nanoparticles after 2 h suggests effective chelation between the silver nanoparticles and the chitosan matrix through coordinate covalent bonding, similar to the approach reported by An and co-workers.[35]

The changes in particle density observed after 6 h are supported by the controlled size distribution (21.29–48.03 nm), indicating a two-step growth process in which silver nanoparticle nucleation occurs first, followed by decoration with WO_3.

This growth mechanism differs from the conventional metal oxide growth pathways reported by Chen and co-workers.[36] The ability of chitosan to provide a suitable chemical environment arises from its polycationic nature. The predominantly spherical morphology of the nanoparticles suggests low surface energy during growth, while their homogeneous dispersion indicates efficient surface stabilization by the hydroxyl and amino functional groups of chitosan. Furthermore, the gradual increase in silver content, as confirmed by EDX analysis, demonstrates that chitosan effectively controls the reduction kinetics, thereby minimizing aggregation compared with the uncontrolled synthesis of silver nanoparticles in the absence of capping agents.[37]

Fig. 3 presents the EDX spectra, elemental mapping and atomic composition of the nanohybrid films formed after 30 min, 2 h and 6 h of reaction. Fig. 3a–c confirm the presence of C, N, O, Ag and W in all the samples, although at different atomic ratios. The EDX spectra also reveal a relatively uniform distribution of tungsten atoms. The time-dependent ability of chitosan to reduce silver ions to silver nanoparticles results in a progressive increase in the percentage of silver detected at longer reaction times.

The nanohybrid film synthesized after 30 min (Fig. 3a) shows the presence of silver; however, the EDX elemental

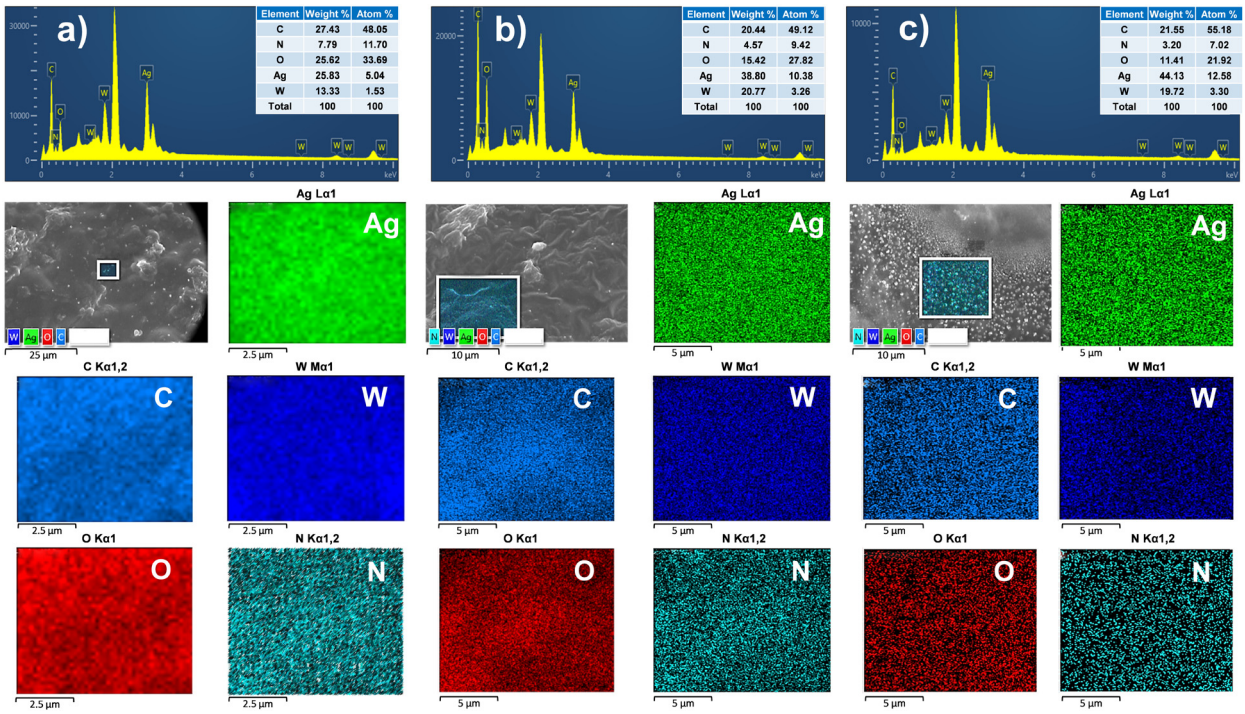

Fig. 3 EDX spectra and corresponding elemental mapping of Ct–$AgWO_3$ films prepared after (a) 30 min, (b) 2 h and (c) 6 h of reaction.

mapping indicates a non-uniform distribution. At, this stage, the tungsten content is relatively low (approximately 13.3 wt%), while silver accounts for 25.8 wt%, suggesting that the reduction process is still incomplete. The slightly scattered elemental distribution implies that the reaction remains in its early stages, and silver nanoparticles have not yet fully formed or dispersed homogeneously within the polymeric matrix. In contrast, the film obtained after 2 h of reaction (Fig. 3b) shows a significant increase in silver content, reaching 38.8 wt%, which indicates that a larger fraction of silver ions has been reduced, resulting in a higher nanoparticle density. The elemental distribution is notably more homogeneous than that observed for the 30 min sample, as observed in the EDX mapping images. In addition, the tungsten content increases to approximately 20.8 wt%, suggesting enhanced incorporation of tungsten oxide into the nanohybrid structure. These results indicate that chitosan promotes the reduction of silver ions, leading to a higher yield of silver nanoparticles that become progressively embedded within the chitosan–tungsten oxide matrix.

For the nanohybrid film formed after 6 h (Fig. 3c), the silver content reaches its highest value at 44.1 wt%, further confirming the progressive and time-dependent reduction of silver ions. This increase is associated with enhanced nanoparticle formation and improved uniform dispersion, reinforcing the structural integrity of the nanohybrid film. The elemental mapping reveals a higher and more uniform dispersion of silver, indicating the formation of a homogeneous nanohybrid film.

The tungsten content remains nearly constant compared to the 2 h sample, showing a slight decrease to 19.7 wt%, which can be attributed to the predominance of silver in the overall composition at longer reaction times. Meanwhile, the carbon content remains nearly constant, suggesting that the chitosan matrix effectively stabilizes nanoparticle formation without undergoing degradation. Overall, the EDX results confirm that longer reaction times enhance silver incorporation and promote improved homogeneity, which is particularly relevant for the antimicrobial performance of the films, as a higher and more uniformly distributed silver content is expected to enhance antimicrobial activity.

It should be noted that SEM provides information primarily on surface morphology and does not allow a definitive determination of the internal structure of the nanocomposite. A more detailed structural characterization (*e.g.*, by TEM or XRD) would be required to fully resolve the internal architecture and phase distribution, which is beyond the scope of the present study.

FTIR analysis

To determine the functional groups present in the synthesized Ct–$AgWO_3$ nanohybrid film, Fourier transform infrared (FTIR) spectroscopy was employed. The FTIR spectra of the synthesized nanohybrid samples (at 30 min, 2 h, and 6 h) in the range of 400–4000 cm^{-1} are shown in Fig. 4. The three sample films displayed similar characteristic peaks to those of chitosan and tungsten oxide, with increasing intensity over reaction time. The stretching vibrations of –OH and –NH groups are responsible for the broad band between 3667 and 3183 cm^{-1}, with a maximum at approximately 3264 cm^{-1}. The peaks at 2933 and 2887 cm^{-1} are assigned to C–H stretching vibrations. The peaks at 1654, 1560, 1387, 1319, 1147, and 1012 cm^{-1} are attributed to the carbonyl group of amides (amide I), N–H bending

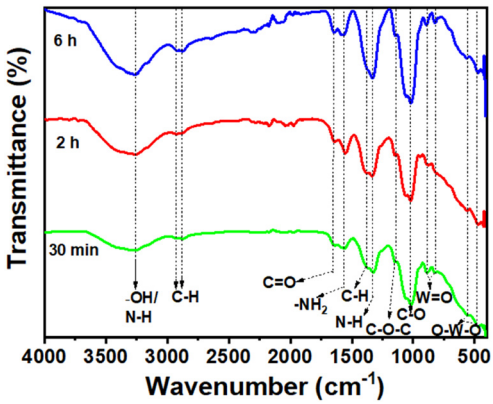

Fig. 4 FTIR spectra of the Ct–$AgWO_3$ nanohybrid films formed after 30 min, 2 h, and 6 h of reaction.

vibrations of amine groups, symmetric deformation modes of CH_3/CH_2 bending vibrations, C–H deformation vibrations associated with amide III N–H, C–O–C vibrations, and C–O stretching vibrations, respectively. The peaks at 882 and 818 cm^{-1} are attributed to W═O vibrations, whereas the O–W–O bond stretching vibrations are responsible for the peaks observed at 559 and 489 cm^{-1}.

These observations, based on FTIR spectral analysis of the Ct–$AgWO_3$ nanohybrid films, indirectly indicate the presence of various molecular interactions and binding phenomena within the composite system. The broad absorption band centered at 3264 cm^{-1} suggests that the chitosan network exhibits a high density of hydrogen bonding involving both –OH and –NH groups. This broadening, compared with the pure chitosan spectra reported by Algethami and co-workers,[38] indicates enhanced intermolecular interactions resulting from silver decoration. Compared with the undecorated systems, the characteristic peaks at 2933 and 2887 cm^{-1} corresponding to the C–H stretching vibrations of chitosan exhibit slight shifts, which may indicate modification of the chitosan backbone through metal coordination.

The appearance of peaks at 882 and 818 cm^{-1}, characteristic of W═O vibrations, along with the O–W–O stretching modes at 559 and 489 cm^{-1}, demonstrates the successful incorporation of tungsten oxide within the chitosan matrix. Variations in these peaks with reaction time are reflected in the relative increase in their intensities, consistent with observations reported by Karimi-Maleh and co-workers[39] in similar metal–oxide systems. The bands attributed to the amide I region (1654 cm^{-1}) and amine group vibrations (1560 cm^{-1}) further confirm coordination interactions between chitosan functional groups and silver and tungsten species. Such interactions are expected to contribute to enhanced mechanical strength and antibacterial properties. This coordination mechanism differs from conventional metal–polymer composite systems described by Vigani and co-workers,[40] suggesting the presence of a three-component interaction that enhances mechanical integrity and may influence antibacterial activity through controlled metal ion release.

XPS analysis

The three synthesized Ct–$AgWO_3$ nanohybrid film samples were characterized by X-ray photoelectron spectroscopy (XPS), and the corresponding spectra are shown in Fig. 5. The XPS survey scan presented in Fig. 5a confirms the presence of O 1s, C 1s, Ag 3d, N 1s, and W 4f peaks. The deconvoluted core-level spectra of the corresponding elements are shown in Fig. 5b–d, respectively. Due to spin–orbit splitting of the W 4f core level,

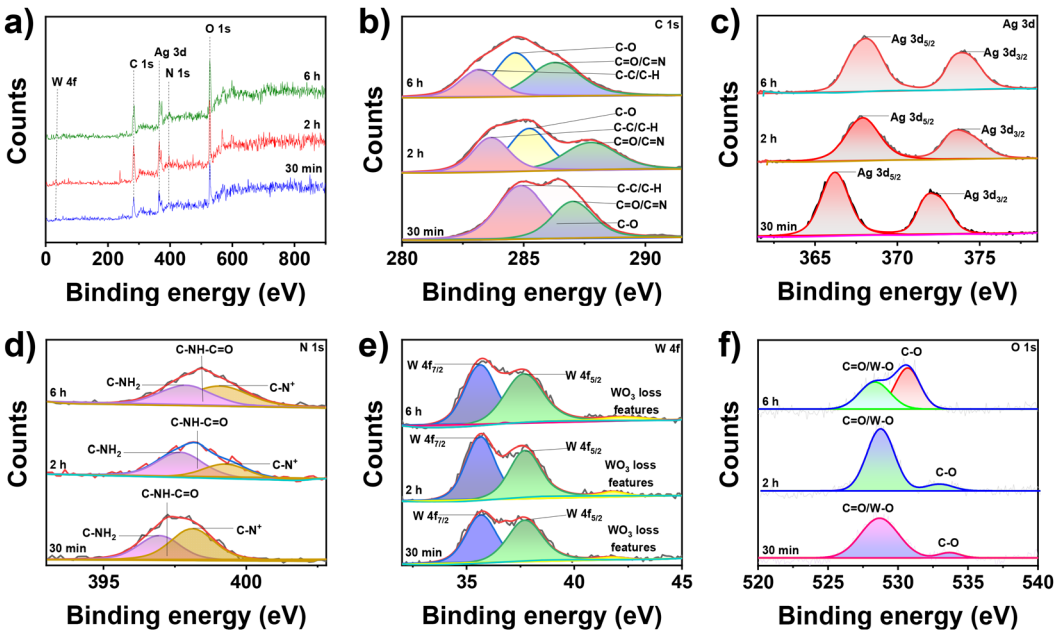

Fig. 5 (a) XPS survey spectra of the Ct–$AgWO_3$ nanohybrid films recorded after 30 min, 2 h, and 6 h of reaction; (b) C 1s, (c) Ag 3d, (d) N 1s, (e) W 4f, and (f) O 1s high-resolution spectra.

the W 4f spectra of the film formed after 6 h exhibit a doublet with binding energies at 35.63 eV (W $4f_{7/2}$) and 37.76 eV (W $4f_{5/2}$). Similar doublets were observed for the 2 h sample at 35.65 and 37.83 eV and for the 30 min sample at 35.67 and 37.80 eV. The close similarity of these peak positions indicates that tungsten exists predominantly in the W^{6+} oxidation state in all three samples, with a characteristic intensity ratio of approximately 4 : 3. The weak feature observed in the 41–42 eV binding energy range corresponds to loss of WO_3. The gradual increase in peak intensity from 30 min to 6 h can be attributed to the time-dependent ability of chitosan to reduce silver ions to metallic silver in the absence of external catalysts.[17]

Detailed XPS analysis reveals the complex nature of the interface at the Ag–WO_3 junction, which is characterized by electronic interactions between silver and tungsten atoms and the formation of localized electronic states. These interactions, manifested as small shifts in binding energies and valence band features, suggest the formation of a composite electronic system that may enhance photocatalytic properties. Notably, this system exhibits different band alignment characteristics compared with conventional Ag–semiconductor interfaces reported by Viorica and co-workers,[41] due to the mediating role of the chitosan matrix. Core-level spectral analysis further provides evidence for the existence of distinct chemical environments at particle surfaces and within the bulk, as well as interface-specific electronic states that differ from those reported by Dickens and co-workers[42] for similar metal–oxide systems. The asymmetry observed in the W 4f spectral region suggests the formation of oxygen vacancies at the interface, which generate localized regions of high electron density and may enhance charge carrier mobility. These XPS features, which evolve with reaction time, indicate complex interfacial synergies between silver reduction kinetics and tungsten oxide structural characteristics, extending beyond the simple surface decoration effects commonly reported in the literature.

The XPS results further confirm the successful incorporation of silver into the WO_3 framework within the chitosan matrix. The consistent presence of Ag 3d peaks in all samples confirms the existence of silver in the nanohybrid films, while the progressive increase in peak intensity with reaction time indicates enhanced reduction of silver ions to metallic silver. Additionally, slight binding energy shifts in the Ag 3d spectra suggest strong electronic interactions between silver and the surrounding matrix components, particularly chitosan and tungsten oxide. The W 4f peaks remain consistent with the W^{6+} oxidation state across all samples, confirming that WO_3 retains its chemical stability throughout the synthesis process. Minor shifts observed in the W 4f and O 1s spectra further indicate electronic interactions between tungsten oxide and embedded silver nanoparticles, supporting the conclusion that silver is not merely adsorbed on the WO_3 surface, but is effectively incorporated into the nanohybrid structure. The C 1s and N 1s spectra provide additional evidence of the role of chitosan in stabilizing silver nanoparticles, as changes in their chemical states indicate strong interactions between the polymer matrix and metal species. In particular, nitrogen-related peaks associated with protonated and amine functionalities confirm that chitosan actively participates in the reduction and stabilization of silver, promoting its uniform dispersion within the WO_3 framework. Moreover, shifts in the O 1s spectra further support the idea that incorporation of silver modifies the electronic environment of WO_3, potentially enhancing the functional performance of the nanohybrid films.

Raman analysis

Raman spectroscopy is an extremely sensitive and powerful technique for identifying structural defects and assessing crystal quality. In this study, Raman analysis was used to confirm the structure of WO_3 and to evaluate the effect of Ag decoration within the chitosan matrix. The Raman spectra were recorded using a laser wavelength of 532 nm (Fig. 6).

The W–O stretching vibrations of WO_3 can be assigned to the peak at 73 cm^{-1}, while the bending vibrations of the bridging oxygen in W–O–W bonds are associated with the peaks at 216 and 337 cm^{-1}.[43] The peaks observed at 547 and 637 cm^{-1}, attributed to the bending vibrations of WO_3, reflect the integrity of the monoclinic crystal structure and the influence of silver decoration on the vibrational modes.[32] The O–W–O stretching vibrations of monoclinic WO_3 can be correlated with the peak at 808 cm^{-1}, whereas the peak at 915 cm^{-1} is characteristic of W═O bonds in the hexagonal WO_3 phase. Among these, the peaks at 73, 216, and 808 cm^{-1} correspond to the major vibrational modes of monoclinic WO_3, while the peak at 547 cm^{-1} is considered a minor mode.[44]

Due to the formation of structural and surface defects, oxygen vacancies, and stoichiometric distortions arising from the mismatch in valence states and ionic radio between Ag^{+}/Ag^{0} and W^{6+} ions, the Ag-decorated samples exhibit noticeable peak shifts and peak broadening.[32] As a result, the WO_3 lattice contains a higher density of oxygen vacancies induced by the incorporation of Ag^{0} and Ag^{+} ions, which enhances the electronic properties of the material. The increase in peak intensity can also be attributed to the higher dopant concentration resulting from the time-dependent reduction of silver ions to silver nanoparticles.

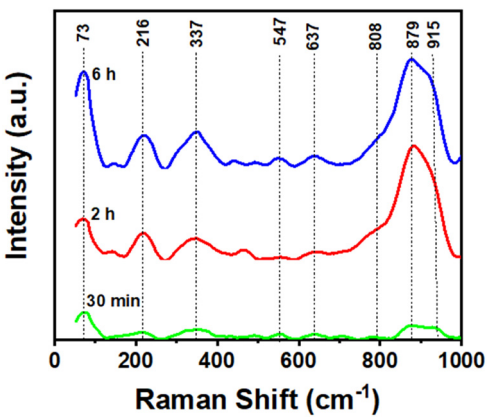

Fig. 6 Raman spectra of the Ct–AgWO_3 nanohybrid films synthesized after 30 min, 2 h, and 6 h of reaction.

Raman spectral analysis further provides insight into the vibrational behavior of the chitosan matrix and the Ag–WO_3 interface. The observed peak broadening and frequency shifts, particularly in the low-frequency region, indicate modifications in WO_3 phonon modes caused by the incorporation of silver, exceeding similar effects reported in other metal–oxide systems by Kirit.[45] The appearance of an additional vibrational mode at 879 cm^{-1}, distinct from the characteristic WO_3 modes, suggests the formation of new chemical interactions at the metal–oxide interface. This interaction may facilitate photon-coupling processes, thereby influencing the electronic and optical properties of the nanohybrid material.

Consistent with the theoretical analysis reported by Scaccabarozzi and co-workers,[46] increased charge transfer is expected in such decorated semiconductor systems. The relative intensities of the W–O–W bridging modes and terminal W═O vibrations provide an indication of the extent of silver decoration, while the presence of combination bands suggests a close interaction between the metal oxide network and the chitosan polymeric backbone. Overall, these vibrational features point to a more complex and synergistic interaction mechanism than those previously reported for similar composite systems.

Thermogravimetric analysis (TGA)

Thermal analysis was performed to evaluate the thermal stability of the synthesized nanohybrid films under temperature variations, highlighting their potential suitability for drug delivery and biomedical applications. The thermal behavior was assessed by thermogravimetric analysis (TGA), and the TGA curves of the three Ct–$AgWO_3$ nanohybrid films were compared with those of chitosan–tungsten oxide (Ct–WO_3) film reported previously (Fig. 7).[47]

Two major weight-loss stages were observed for all samples. The films synthesized after 6 h, 2 h, and 30 min exhibited an initial weight loss of approximately 13% between 0 °C and 102 °C, whereas the Ct–WO_3 film showed a weight loss of about 12% between 0 °C and 139 °C. This initial weight loss is attributed to the removal of physically adsorbed moisture, indicating relatively low hydration, which is a desirable feature for maintaining thermal stability in biomedical applications. The occurrence of dehydration at lower temperatures in the Ct–$AgWO_3$ samples suggests the effect of silver decoration, which likely reduces the accessibility of hydrophilic active sites.[48]

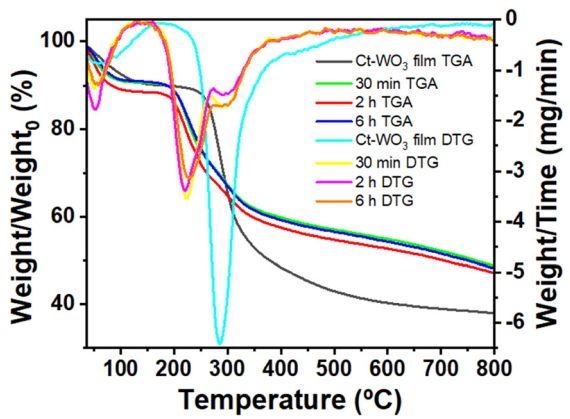

Fig. 7 TGA curves of the Ct–$AgWO_3$ nanohybrid films synthesized after 30 min, 2 h, and 6 h, compared with the Ct–WO_3 film.

The second major weight-loss step occurred between 200 and 450 °C for the Ct–$AgWO_3$ nanohybrid films, while for the Ct–WO_3 film it was observed between 240 and 450 °C. At 800 °C, the total weight losses for the 6 h, 2 h, 30 min, and Ct–WO_3 films were 51.30%, 51.30%, 53.05%, and 62.06%, respectively. This noticeable difference demonstrates that the thermal stability of the chitosan–tungsten oxide film is significantly enhanced upon decoration with silver nanoparticles.

Overall, the chitosan–silver-decorated tungsten oxide nanohybrid films exhibit superior thermal stability compared to the undecorated chitosan–tungsten oxide film, as evidenced by their higher degradation onset temperatures and lower total weight loss. The incorporation of silver into the WO_3–chitosan matrix reinforces the hybrid structure, reducing the rate of thermal degradation. Differential thermogravimetric analysis (DTG) further confirms the presence of distinct degradation steps, with the main weight-loss peaks shifting toward higher temperatures in the silver-decorated samples, indicating enhanced thermal resistance.

Comparative analysis of the TGA and DTG results suggests that incorporation of silver plays a key role in improving the thermal stability of the nanohybrid films. In contrast, the Ct–WO_3 film, which lacks silver, exhibits lower thermal resistance and greater weight loss at lower temperatures, likely due to the limited structural reinforcement provided by tungsten oxide alone. The delayed thermal decomposition observed for the silver-decorated films indicates stronger interfacial interactions among chitosan, silver, and tungsten oxide components.

The stabilizing effect of silver is attributed to its ability to enhance structural rigidity and interfacial bonding within the hybrid matrix, effectively acting as a thermal barrier that slows polymer degradation.[49,50] Similar behavior has been reported in previous studies, where noble metal decoration in polymer–metal oxide hybrids improved thermal resistance through enhanced metal dispersion and stronger polymer–metal interactions. Additionally, silver nanoparticles are known to improve thermal stability by restricting polymer chain mobility and delaying the degradation of the polymeric phase, as previously observed in other chitosan-based metal nanocomposite systems.[51]

Overall, the enhanced thermal stability of the chitosan–silver-decorated tungsten oxide nanohybrid films, compared to the pristine chitosan–tungsten oxide film, is attributed to the synergistic effects of incorporation of silver and tungsten oxide reinforcement within the chitosan matrix.[52,53]

Analysis of photoluminescence spectra

The photoluminescence (PL) properties of the prepared nanohybrid film samples were investigated to gain insight into the band gap, oxygen deficiency, impurity energy levels, and surface defects of the semiconducting oxide present in the system (Fig. 8). The de-excitation process from the conduction band

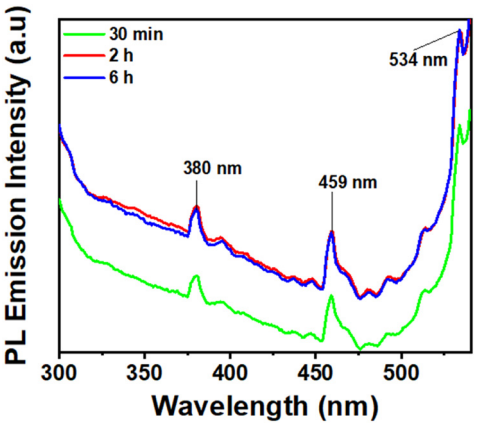

Fig. 8 Photoluminescence spectra comparing the emission of the nanohybrid films synthesized after 30 min, 2 h, and 6 h at an excitation wavelength of 280 nm and emission wavelengths between 300 and 540 nm.

(CB; W^{6+}, 4f) to the valence band (O 2p) leads to the appearance of a broad emission peak with a maximum at 459 nm, which is attributed to band-edge transitions. This emission is associated with an energy level of approximately 2.7 eV and reflects radiative recombination processes influenced by charge transfer interactions among WO_3, Ag, and the chitosan matrix within the hybrid structure.

The emission peak observed at 380 nm is associated with defect-related states, particularly oxygen vacancies. Additionally, the peak detected at 534 nm is also associated with V_0^+ oxygen vacancy–related states. Variations in PL intensity among samples cast after different reaction times (30 min, 2 h, and 6 h) indicate modifications in the electronic structure and defect density. Notably, the samples prepared after 2 h and 6 h exhibit higher PL intensities than the 30 min sample, which may be associated with increased radiative recombination pathways and defect-related emissions. This behavior is likely to be related to enhanced Ag–WO_3 interactions and the stabilization of defect sites with prolonged reaction time. It should be noted that the PL spectra were not normalized with respect to absorbance at the excitation wavelength. Therefore, the PL results are interpreted qualitatively in terms of emission pathways rather than as a direct measure of recombination efficiency.

The prominent emission centered at 459 nm corresponds to characteristic band gap transitions of WO_3-based nanostructures, which are commonly reported for tungsten oxide nanocomposites and fall within the visible region.[54] Silver decoration plays a significant role in modifying the optical properties of the nanohybrid films. The incorporation of Ag nanoparticles induces localized surface plasmon resonance (LSPR) effects, which can either enhance or quench PL emissions, depending on their interaction with the WO_3 matrix. The observed PL behavior suggests that Ag nanoparticles promote charge transfer processes, highlighting the potential of the Ct–$AgWO_3$ nanohybrid films for optoelectronic and photocatalytic applications. Compared to undecorated WO_3 films, which typically display PL emissions in the blue region (*ca.* 420–460 nm) associated with oxygen vacancy states, the Ct–$AgWO_3$ nanohybrid films exhibit a redistribution of emission intensity, reflecting the influence of silver incorporation on the electronic structure.

The chitosan matrix acts as both a reducing and stabilizing agent during the formation of the nanohybrid film. Its functional groups can coordinate with metal ions, facilitating the formation and stabilization of metal nanoparticles within the polymeric matrix, influencing the optical properties of the resulting composites. Previous studies have shown that the incorporation of semiconductor nanocrystals into chitosan-based biopolymer systems leads to materials with distinct PL characteristics. In the present Ct–$AgWO_3$ nanohybrid films, chitosan likely plays a crucial role in stabilizing Ag nanoparticles and maintaining a uniform film structure, which significantly affects the observed PL behavior.[55]

Similar trends have been reported for other chitosan-based nanocomposites with tunable PL properties depending on their composition and synthesis conditions. For example, chitosan/poly(vinyl alcohol)/ZnO nanocomposite films have shown enhanced PL intensity and redshifted emission compared to chitosan-based films without ZnO nanoparticles, emphasizing the role of metal oxides in modulating optical behavior.[56] Furthermore, the incorporation of reduced graphene oxide or carbon nanotubes into chitosan matrices has been reported to improve both electrical conductivity and photoluminescence properties. These findings highlight the versatility of chitosan as a functional matrix for designing nanocomposites with tailored optical characteristics.

The proposed photocatalytic mechanism of the prepared nanohybrid material is illustrated in Fig. 9. When photons with energy equal to or greater than the band gap energy of the nanomaterial irradiate the catalyst surface, photoexcitation occurs, generating electrons in the conduction band and holes in the valence band.[57,58] The photogenerated electrons can react with dissolved oxygen to form superoxide radical anions ($O_2^{\bullet -}$), reactive oxygen species (ROS), or hydrogen peroxide (H_2O_2). Simultaneously, the holes in the valence band interact with water molecules or hydroxide ions (OH^-) to generate hydroxyl radicals ($OH^{\bullet}$).

These reactive species, including H^+, $O_2^{\bullet -}$, $OH^{\bullet}$, and H_2O_2, play a crucial role in the photocatalytic process and induce oxidative stress in biological systems, ultimately leading to cell

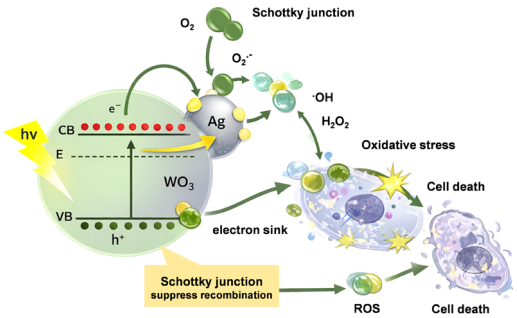

Fig. 9 Illustration of a plausible photocatalytic mechanism of silver and tungsten oxide in the nanohybrid film.

death *via* necrosis or apoptosis. The presence of silver may contribute to interfacial charge transfer process at the Ag–WO_3 interface, trapping photogenerated electrons and suppressing electron–hole recombination. However, a detailed assessment of charge-carrier dynamics would still require time-resolved photoluminescence or transient spectroscopic techniques, which are beyond the scope of the present work.

Owing to the difference in work function between Ag and WO_3, photogenerated electrons tend to migrate from Ag to the conduction band of WO_3, resulting in band bending and the formation of a space-charge region. This charge separation enhances the lifetime of photogenerated carriers, enabling efficient redox reactions and promoting the generation of ROS, which underpins the photocatalytic and bioactive performance of the Ct–$AgWO_3$ nanohybrid films.

Conclusions

To investigate the effect of reaction time on the morphology, growth process, and structural and optical properties of the samples, Ct–$AgWO_3$ nanohybrid films were successfully fabricated *via* a green synthesis and reduction approach at reaction times ranging from 30 min to 6 h. The presence of tungsten oxide within the chitosan matrix under all investigated conditions was confirmed by FTIR analysis. The FTIR spectra of samples prepared at different hydrothermal reaction times showed increasing peak intensities over time, indicating the influence of the incorporation of silver nanoparticles.

Distinct morphological evolutions were observed with increasing reaction time, including agglomerated spherical particles at 30 min, relatively well-dispersed and sparse particles after 2 h, and well-dispersed, densely populated particles after 6 h. These morphological changes are attributed to limited reaction time during the initial stages of silver reduction and a lower availability of silver nanoparticles for decorating WO_3 within the polymer matrix. As the reaction time increased, the particle size initially decreased and subsequently increased.

Overall, the synthesized Ct–$AgWO_3$ nanohybrid material exhibits effective structural, optical, and functional properties. The time-dependent synthesis resulted in spherical nanoparticles with a narrow size distribution (21.29–48.03 nm) and improved thermal stability up to 800 °C. The material showed strong optical activity in the 400–500 nm region and efficient charge transfer behavior, as evidenced by the retention of the W^{6+} oxidation state and controlled silver decoration. The results suggest potential improvements in the optical and functional properties due to Schottky junction formation under UV-light irradiation. Owing to its multifunctional properties, the green-synthesized Ct–$AgWO_3$ nanohybrid film shows strong potential for applications in antimicrobial coatings, photocatalytic water treatment, medical devices, self-cleaning materials, and food packaging. Its potent antibacterial activity, controlled silver release, thermal stability, and uniform film-forming ability further support its suitability for medical textiles, protective packaging, and coatings for biomedical and industrial applications.

Author contributions

Shephrah Olubusola Ogungbesan: conceptualization, data curation, research design, formal analysis, investigation, methodology, project administration, writing of original draft, reviewing and editing. Oluwaseun Hanah Anselm: visualization, writing, reviewing and editing. Eduardo Buxaderas: conceptualization, reviewing and editing. Yanina Moglie: conceptualization, reviewing and editing. César Saldías: conceptualization, reviewing and editing. Mulenga Kalulu: reviewing and editing, Rosemary Anwuli Adedokun: resources, investigation, Enock Olugbenga Dare: reviewing and editing, Michael Olawale Daramola: reviewing and editing. David Díaz Díaz: conceptualization, funding acquisition, visualization, supervision, reviewing and editing. Guodong Fu: conceptualization, funding acquisition, resource supervision, validation, project administration.

Conflicts of interest

There are no conflicts to declare.

Data availability

The data that support the findings of this study are available from the corresponding author upon reasonable request.

Supplementary information (SI) is available. See DOI: https://doi.org/10.1039/d6cp00607h.

Acknowledgements

This work was supported by the National Natural Science Foundation of China under Grant 52073059. S. O. O. wishes to especially thank Mr Sanjo Emmanuel Somefun for his recognition of support and contribution to the success of this work. D. D. D. acknowledges the Fundación Ramón Areces, Ministry of Science and Innovation (PID2022-142118OB-I00/AE/10.13039/501100011033/UE), and Cátedra Institucional de Medio Ambiente y Desarrollo Sostenible Cabildo de Tenerife-Universidad de La Laguna (MADS26.L1.04) for financial support, and Nanotec, INTech, Cabildo de Tenerife and ULL for laboratory facilities.

References

1 M. Dadkhah and J. M. Tulliani, *Sensors*, 2022, **22**, 4669.
2 N. E. Fard, I. Raeisi, Z. Yousefipour and R. Mosavin, *ACS Appl. Nano Mater.*, 2024, **7**, 5698–5728.
3 G. Paramasivam, V. V. Palem, S. Meenakshy, L. K. Suresh, M. Gangopadhyay, S. Antherjanam and A. K. Sundramoorthy, *Colloids Surf., B*, 2024, 114032.
4 A. Sharma, A. K. Saini, N. Kumar, N. Tejwan, T. A. Singh, V. K. Thakur and J. Das, *Surf. Interfaces*, 2022, **28**, 101641.
5 J. Gutpa, H. Shaik, K. Naveen Kumar and S. A. Sattar, *Mater. Sci. Semicond. Process.*, 2022, **143**, 106534.
6 I. Şerban and A. Enesca, *Front. Chem.*, 2020, **8**, 1–8.

7 W. Zhang, Y. Qi, L. Zhang, Y. Tang, C. Qi, Q. Shen, Y. Ma and B. Wang, *Surf. Coat. Technol.*, 2022, **434**, 128165.
8 H. Yang, H. Sun, Q. Li, P. Li, K. Song, B. Song and L. Wang, *Vacuum*, 2019, **164**, 411–420.
9 X. Li, L. Fu, H. Karimi-Maleh, F. Chen and S. Zhao, *Heliyon*, 2024, 38515674.
10 M. Salot, K. Santhy, D. Mandal, A. K. Pramanick, B. Rajasekaran, G. Avasthi and S. K. Chaudhury, *Int. J. Appl. Ceram. Technol.*, 2025, e15080.
11 W. Wang, H. Wen, X. Huan, J. Shi, Z. Li, J. Su and C. Wang, *Mater. Des.*, 2020, **186**, 108351.
12 Z. Hou, C. Cui, Y. Yang, Z. Huang, Y. Zhuang, Y. Zeng and T. Zhang, *Small*, 2024, **20**, 2407167.
13 O. Samuel, M. H. D. Othman, R. Kamaludin, O. Sinsamphanh, H. Abdullah, M. H. Puteh and T. A. Kurniawan, *Ceram. Int.*, 2022, **48**, 5845–5875.
14 Y. Zhu, C. Chen, H. Mu, R. Gao, X. Deng, W. Cai, C. Fu, G. Chen, Z. Wang and X. Lei, *J. Mater. Sci.: Mater. Electron.*, 2024, **35**, 1–25.
15 D. Kiani, S. Sourav, W. Taifan, M. Calatayud, F. Tielens, I. E. Wachs and J. Baltrusaitis, *ACS Catal.*, 2020, **10**, 4580–4592.
16 S. Liang, G. Liao, W. Zhu and L. Zhang, *Biomater. Res.*, 2022, **26**, 1–21.
17 Y. Liu, S. Wu, Y. Liu, H. Zhang, M. Zhang, Z. Tang, Y. Wang, T. Gong, Z. Yao, X. Fang and W. Bu, *Biomaterials*, 2020, **234**, 119762.
18 A. C. Burdușel, O. Gherasim, A. M. Grumezescu, L. Mogoantă, A. Ficai and E. Andronescu, *Nanomaterials*, 2018, **8**, 1–25.
19 M. T. Ramesan and V. Santhi, *Compos. Interfaces*, 2018, **25**, 725–741.
20 S. Raza, A. Ansari, N. N. Siddiqui, F. Ibrahim, M. I. Abro and A. Aman, *Sci. Rep.*, 2021, **11**, 1–15.
21 V. Holubnycha, Y. Husak, V. Korniienko, S. Bolshanina, O. Tveresovska, P. Myronov, M. Holubnycha, A. Butsyk, T. Borén, R. Banasiuk and A. Ramanavicius, *Nanomaterials*, 2024, **14**, 137.
22 Y. N. Kanafin, A. Abduvalov, M. Kaikanov, S. G. Poulopoulos and T. S. Atabaev, *Heliyon*, 2024, **11**, e40788.
23 S. O. Ogungbesan, O. Ejeromedoghene, Y. Moglie, E. Buxaderas, B. Cui, R. A. Adedokun, M. Kalulu, M. A. Idowu, D. Díaz Díaz and G. Fu, *New J. Chem.*, 2024, **48**, 15428–15435.
24 S. M. Park, Y. C. Nah and C. Nam, *J. Nanosci. Nanotechnol.*, 2017, **17**, 7719–7722.
25 S. O. Ogungbesan, E. Buxaderas, R. A. Adedokun, Y. Moglie, S. Grijalvo, M. T. García, C. Bingbing, D. Díaz Díaz and G. Fu, *ChemistrySelect*, 2024, **9**, 1–9.
26 P. Meng, J. Huang and X. Liu, *Appl. Surf. Sci.*, 2019, **465**, 125–135.
27 M. I. Din, R. Khalid and Z. Hussain, *Anal. Lett.*, 2018, **51**, 892–907.
28 M. Singh, M. Goyal and K. Devlal, *J. Taibah Univ. Sci.*, 2018, **12**, 470–475.
29 T. Ali, A. Ahmed, U. Alam, I. Uddin, P. Tripathi and M. Muneer, *Mater. Chem. Phys.*, 2018, **212**, 325–335.
30 E. Umar, M. Ikram, A. Haider, A. Shahzadi and A. Ul-Hamid, *Surf. Interfaces*, 2023, **38**, 102835.
31 S. Ghazal, M. Mirzaee, M. Darroudi, Z. Sabouri and S. Khadempir, *J. Photochem. Photobiol., A*, 2024, **448**, 115323.
32 B. Harikumar, M. K. Okla, S. Kokilavani, B. Almunqedhi, R. Alshuwaish, M. A. Abdel-Maksoud, M. A. El-Tayeb and S. S. Khan, *J. Clean. Prod.*, 2023, **398**, 136549.
33 C. Zhou, M. Wang and F. Yang, *Ceram. Int.*, 2024, **50**, 35869–35901.
34 Z. Zaheer, *J. Polym. Res.*, 2021, **28**, 348.
35 J. An, G. Guo, R. Yin, Q. Luo, X. Li, F. Liu and D. Wang, *Polym. Int.*, 2018, **67**, 515–527.
36 Y. Chen, Y. Liu, Q. Dong, C. Xu, S. Deng, Y. Kang, M. Fan and L. Li, *Int. J. Biol. Macromol.*, 2023, **235**, 123716.
37 A. Dhaka, S. Chand Mali, S. Sharma and R. Trivedi, *Results Chem.*, 2023, **6**, 101108.
38 N. Algethami, A. Rajeh, H. M. Ragab, A. E. Tarabiah and F. Gami, *J. Mater. Sci.: Mater. Electron.*, 2022, **33**, 10645–10656.
39 H. Karimi-Maleh, B. G. Kumar, S. Rajendran, J. Qin, S. Vadivel, D. Durgalakshmi, F. Gracia, M. Soto-Moscoso, Y. Orooji and F. Karimi, *J. Mol. Liq.*, 2020, **314**, 113588.
40 B. Vigani, S. Rossi, G. Sandri, M. C. Bonferoni, C. M. Caramella and F. Ferrari, *Expert Opin. Drug Delivery*, 2019, **16**, 715–740.
41 G. P. Viorica, V. Musat, A. Pimentel, T. R. Calmeiro, E. Carlos, L. Baroiu, R. Martins and E. Fortunato, *J. Alloys Compd.*, 2019, **803**, 922–933.
42 C. F. Dickens, J. H. Montoya, A. R. Kulkarni, M. Bajdich and J. K. Nørskov, *Surf. Sci.*, 2019, **681**, 122–129.
43 W. Song, R. Zhang, X. Bai, Q. Jia and H. Ji, *J. Mater. Sci.: Mater. Electron.*, 2020, **31**, 610–620.
44 G. Mathankumar, P. Bharathi, M. K. Mohan, J. Archana, S. Harish and M. Navaneethan, *Sens. Actuators, B*, 2022, **353**, 131057.
45 M. Abbas, N. Hussain Shah, M. Qasim, M. Imran, M. Sulaman, N. Ahmad, M. Lauqman, M. Ashfaq Ahmad, Y. Cui and Y. Wang, *J. Ind. Eng. Chem.*, 2024, **130**, 521–532.
46 A. D. Scaccabarozzi, A. Basu, F. Aniés, J. Liu, O. Zapata-Arteaga, R. Warren, Y. Firdaus, M. I. Nugraha, Y. Lin, M. Campoy-Quiles, N. Koch, C. Müller, L. Tsetseris, M. Heeney and T. D. Anthopoulos, *Chem. Rev.*, 2022, **122**, 4420–4492.
47 A. A. Keshk, A. Abu-Rayyan, N. H. Elsayed, M. Al-Anazi, S. Said, N. A. Alamrani, R. M. El-Shabasy and K. R. Shoueir, *Biomass Convers. Biorefin.*, 2024, **14**, 19529–19539.
48 I. A. Udoetok, A. H. Karoyo, M. H. Mohamed and L. D. Wilson, *Molecules*, 2024, **29**, 445.
49 S. Xing, Z. Pan, X. Wu, H. Chen, X. Lv, P. Li, J. Liu and J. Zhai, *J. Mater. Chem. C*, 2020, **36**, 12607–12614.
50 Z. Ji, L. Zhang, G. Xie, W. Xu, D. Guo, J. Luo and B. Prakash, *Friction*, 2020, **8**, 813–846.
51 X. Zhang, Y. Chen, L. Lian, Z. Zhang, Y. Liu, L. Song, C. Geng, J. Zhang and S. Xu, *Nano Res.*, 2021, **14**, 628–634.
52 R. H. Zhang, X. T. Shi, L. Tang, Z. Liu, J. L. Zhang, Y. Q. Guo and J. W. Gu, *Chin. J. Polym. Sci.*, 2020, **38**, 730–739.

53 T. M. Majka, A. Leszczyńska and K. Pielichowski, *Polymer Nanocomposites: Electrical and Thermal Properties*, Springers, 2016, pp. 167–190.
54 S. Ramkumar and G. Rajarajan, *J. Mater. Sci.: Mater. Electron.*, 2016, **27**, 12185–12192.
55 N. Slyusarenko, M. Gerasimova, A. Plotnikov, N. Gaponik and E. Slyusareva, *Phys. Chem. Chem. Phys.*, 2019, **9**, 4831–4838.
56 S. Kumar, B. Krishnakumar, A. J. Sobraland and J. Koh, *Carbohydr. Polym.*, 2019, **205**, 559–564.
57 D. E. Lee, M. K. Kim, M. Danish and W. K. Jo, *Catal. Commun.*, 2023, **183**, 106764.
58 M. A. Hassaan, M. A. El-Nemr, M. R. Elkatory, S. Ragab, V. C. Niculescu and A. El Nemr, *Top. Curr. Chem.*, 2023, **381**, 31.